Journal of Alloys and Compounds 848 (2020) 156378

Contents lists available at ScienceDirect

Journal of Alloys and Compounds

journal homepage: http://www.elsevier.com/locate/jalcom

Microstructural stability and mechanical behavior of a Co–20Ni–7Al–7W–4Ti at.% superalloy

Chunan Li [a], Ding-Wen Chung [a], David C. Dunand [a], David N. Seidman [a, b, *]

[a] Northwestern University, Department of Materials Science and Engineering, 2220 Campus Drive, Evanston, IL, 60208-3108, USA
[b] Northwestern University Center for Atom-Probe Tomography, 2220 Campus Drive, Evanston, IL, 60208-3108, USA

ARTICLE INFO

Article history:
Received 7 April 2020
Received in revised form
6 July 2020
Accepted 11 July 2020
Available online 23 July 2020

Keywords:
Cobalt alloys
Superalloy
Coarsening
Creep
Rafting

ABSTRACT

The temporal evolution of the microstructure and microhardness of a polycrystalline $L1_2$-strengthened Co-based superalloy (Co–19.6Ni–7.6Al–7.4W–4.1Ti, at.%) was investigated for an aging temperature of 900 °C. The γ(f.c.c.)/γ′($L1_2$) structure remained stable throughout aging to the longest aging time of 2000 h (83 days), with no additional phases present. While the volume fraction of γ′($L1_2$)-precipitates reached an almost constant value of 64% at 16 h, the temporal evolution of the γ′($L1_2$)-precipitates' mean-radius and their number density (temporal exponent of $p = 3.49 \pm 0.18$ for the equivalent radius, and $q = -0.74 \pm 0.04$ for the volumetric number density) deviated somewhat from the Lifshitz-Slyozov (LS) predictions ($p = 3$ and $q = -1$), suggesting that the alloy had not achieved a true stationary-state at 2000 h. At ambient temperature, a peak Vickers microhardness of 3.80 ± 0.10 GPa was achieved after 240 h of aging. As the testing temperature was increased, an anomalous increase in flow-stress was also observed, with a peak flow-stress value of 705 MPa measured at 750 °C, 30 MPa higher than an archival literature value with about half the Ni concentration (10 at.%). Creep resistance at 850 °C was greater than an archival literature value for a ternary Co–9Al–9W alloy. After 200 h of compressive creep at 850 °C the microstructure evolved as follows: (i) the volume fraction of the γ′($L1_2$)-phase increased from 64% to 79%; and (ii) some grains exhibited rafts of γ′($L1_2$)-precipitates along ⟨100⟩-directions. While the first change is expected to improve creep resistance, the second one is deleterious, as evidenced by a comparison with the creep resistance of a sample without rafts of γ′($L1_2$)-precipitates tested for the same conditions.

© 2020 Elsevier B.V. All rights reserved.

1. Introduction

The discovery of a γ(f.c.c.)/γ′($L1_2$) microstructure in the Co–Al–W ternary system, with the solidus and liquidus temperatures being 50–150 °C higher than that of Ni-based superalloys, has made Co-based superalloys attractive for use as blade and disk materials in next-generation gas-turbines [1,2]. Co-based superalloys exhibit a flow-stress anomaly analogous to Ni-based superalloys [3], with a high-temperature flow-stress and creep-resistance comparable to first-generation Ni-based superalloys, without being heavily alloyed [4]. Furthermore, many solute atoms have a smaller diffusivity in Co than in Ni, suggesting that diffusion-controlled processes (coarsening and creep) should be slower in Co-based superalloys [5]. Single-crystals of a Co–Al–W-based alloy have been successfully grown without freckle-formation and limited macro-segregation [6], which are encouraging observations for straightforward processing.

Unfortunately, the small γ(f.c.c.)/γ′($L1_2$) two-phase region in the Co–Al–W system only allows limited composition variations before the precipitation of deleterious topologically close-packed (TCP) phases [1]. Moreover, first-principles calculations predict a lack of stability for $Co_3(Al_{0.5},W_{0.5})(L1_2)$ at 0 K [7]. The metastability of $Co_3(Al_{0.5},W_{0.5})$ was confirmed experimentally by observations of β-CoAl (B2) and χ-$Co_3W(D0_{19})$, after extended aging at 900 °C [8,9]. A further weakness is that the γ′($L1_2$)-solvus-temperature in a Co–Al–W ternary alloy (1000 °C [1]) is lower than in Ni-based superalloys, which greatly reduces its high-temperature strength. Alloying with Ni or Ti expands and stabilizes the γ′($L1_2$)-phase-field [8,10,11], with a concomitant increase in the γ′($L1_2$)-volume-fraction [12,13]. Addition of Ni [11], Ti [8], and other elements, such as Ta and Nb [14], can also result in significant increases in the γ′($L1_2$)-

* Corresponding author. Northwestern University, Department of Materials Science and Engineering, 2220 Campus Drive, Evanston, IL, 60208-3108, USA.
E-mail address: d-seidman@northwestern.edu (D.N. Seidman).

https://doi.org/10.1016/j.jallcom.2020.156378
0925-8388/© 2020 Elsevier B.V. All rights reserved.

Nomenclature

A	pre-exponential factor in the Norton power law for secondary creep at constant temperature
A_{eq}	circular-equivalent area of a $\gamma'(L1_2)$-precipitate
a^{γ}	lattice parameter of the γ(FCC)-phase
$a^{\gamma'}$	lattice parameter of the $\gamma'(L1_2)$-phase
K	coarsening rate constant in the LS and P–V models
$N_A(t)$	areal number density of $\gamma'(L1_2)$-precipitates at time t
$N_V(t)$	volumetric number density of $\gamma'(L1_2)$-precipitates at time t
n	apparent stress exponent in the Norton power law for secondary creep at constant temperature
p	temporal exponent for $\langle R(t)\rangle$
q	temporal exponent for $N_V(t)$
$\langle R(t)\rangle$	mean circular-area-equivalent radius of all $\gamma'(L1_2)$-precipitates at time t
R	circular-area-equivalent radius of each $\gamma'(L1_2)$-precipitate
$\langle R(t_0)\rangle$	mean circular-area-equivalent radius of all $\gamma'(L1_2)$-precipitates at the onset of quasi-stationary coarsening at time t_0
t	aging time
t_0	time at the onset of quasi-stationary coarsening
γ	face-centered cubic (f.c.c.) phase
γ'	$Co_3(Al_{0.5},W_{0.5})(L1_2)$-type phase
δ	γ(f.c.c.)/$\gamma'(L1_2)$-lattice-parameter misfit
$\dot{\varepsilon}$	minimum strain rate in the Norton power law for secondary creep at constant temperature
ξ^2	coefficient of determination
$\varphi^{\gamma'}(t)$	volume fraction of $\gamma'(L1_2)$-precipitates in percentage at time t
$\varphi^{\gamma'}_{eq}$	equilibrium volume fraction of $\gamma'(L1_2)$-precipitates in percentage
APB	anti-phase boundary
CSF	complex stacking fault
EDM	electro-discharge machining
EDS	energy-dispersive X-ray spectroscopy
GB	grain-boundary
LS	Lifshitz-Slyozov
P–V	Philippe-Voorhees
RMS	root-mean-square
SEM	scanning electron microscopy
SISF	superlattice intrinsic stacking fault
TCP	topologically close-packed

solvus-temperature.

The ability to withstand high mechanical loads at elevated temperature is crucial for gas-turbine blade applications. Whereas, Ni increases the $\gamma'(L1_2)$-volume-fraction and strengthens Co-based superalloys, it can also increase the interdiffusion coefficients [15], which leads to faster coarsening kinetics [16]. As a result, the creep resistance of Co–Ni–Al–W alloys is similar to that of ternary Co–Al–W alloys [12]. In contrast, the addition of Ti increases both the creep-resistance [13] and the flow-stress [17,18]. Thus, adding both Ni and Ti to Co–Al–W alloy yields a relatively simple quinary Co–Ni–Al–W–Ti alloy, as studied herein, which is a first step toward understanding the interplay among alloying elements, while acknowledging that an optimized Co-based superalloy compositions will probably require ten or more alloying elements, as is the case for all commercial Ni-based superalloys [19,20].

Microstructural evolution during creep, such as rafting of $\gamma'(L1_2)$ precipitates, also affects the mechanical behavior of superalloys [21–24]. Ni-based superalloys typically exhibit a negative γ(f.c.c.)/$\gamma'(L1_2)$-lattice-parameter misfit, defined by

$$\delta = 2\frac{a^{\gamma'} - a^{\gamma}}{a^{\gamma'} + a^{\gamma}} \quad (1)$$

where $a^{\gamma'}$ and a^{γ} are the lattice parameters of the $\gamma'(L1_2)$ and γ(f.c.c.)-phases, respectively. In contrast, Co-based superalloys possess a positive lattice-parameter misfit [25–27], which has been proposed to be beneficial for high-temperature creep- and fatigue-resistances [28]. A positive lattice-parameter misfit causes a reduction in the compressive stresses in the vertical γ(f.c.c.)-channels, while increasing them in the horizontal-direction. Dislocations created by enhanced-creep [29,30] in the horizontal γ(f.c.c.)-channels can then enter the γ(f.c.c.)/$\gamma'(L1_2)$-heterophase-interfaces, thereby accommodating the lattice-parameter misfit and relieving the elastic strain-energy [31]. The vertical γ(f.c.c.)-channels will, however, remain elastically strained and therefore become energetically unfavorable [32]. As a result, the $\gamma'(L1_2)$-precipitates coagulate and coalesce to form plate-like structures in a direction normal to the compressive loading, which is denoted an N-type raft.

The present study investigates the microstructural evolution and mechanical behavior of a model polycrystalline Co-based superalloy (Co–20Ni–7Al–7W–4Ti), where all the elemental concentrations are henceforth given in at.%. To characterize the long-term microstructural stability, the γ(f.c.c.)/$\gamma'(L1_2)$ microstructure was evaluated employing scanning electron microscopy (SEM) after different aging times. Additionally, the $\gamma'(L1_2)$-precipitate-morphology was quantified stereologically in the quasi-stationary coarsening regime, where the $\gamma'(L1_2)$-volume-fraction, $\varphi^{\gamma'}$, is asymptotically slowly approaching a constant value. The measured coarsening kinetics were compared to mean-field models, including the Lifshitz-Slyozov (LS) [33,34] and Philippe-Voorhees (P–V) [35] models, and the mechanical behavior of the alloy was investigated utilizing Vickers microhardness, compressive flow-stress measurements, and compressive creep-tests. The evolution of the microstructure after creep was compared with the pre-creep microstructure by SEM imaging.

2. Experimental procedures

Ingots were produced by arc-melting high-purity constituent elements (99.9+% Co, 99.99% Ni, 99.99% Al, 99.97% W, 99.99% Ti, from Alfa Aesar) under an argon atmosphere (eight flips, remelted, and solidified in a cold copper-hearth), homogenized at 1250 °C for 24 h in evacuated quartz capsules, which was followed by water-quenching. The homogenized samples were then aged at 900 °C in evacuated quartz capsules for times ranging from 4 h to 2000 h, again followed by water-quenching. Cylindrical (10 mm in height, 5 mm in diameter) mechanical test samples were prepared by electro-discharge machining (EDM) from an ingot aged for 240 h.

The homogenized and aged samples were mounted and chemically etched for 5 s using Carapella's reagent (10 g $FeCl_3 \cdot 6H_2O$, 4 mL HCl, and 200 mL of methanol) and then imaged using a Hitachi SU8030 SEM equipped with an Oxford INCAx-act energy-dispersive X-ray spectroscopy (EDS) detector.

NIH ImageJ (version 1.50i) was used to measure the radii of the $\gamma'(L1_2)$-precipitates (circular-area-equivalent radii, $R = \sqrt{A_{eq}/\pi}$,

where A_{eq} is the measured circular-equivalent area), volume fraction, $\varphi^{\gamma'}$, and the areal number density of precipitates, N_A. To ensure statistical significance, 600 to 3000 precipitates were sampled for each aging condition. The volumetric number density of $\gamma'(L1_2)$-precipitates was calculated employing the stereological relationship [36]:

$$N_V = \frac{N_A}{2\langle R\rangle} \tag{2}$$

where $\langle R\rangle$ is the mean-value of the circular-area-equivalent radii of $\gamma'(L1_2)$-precipitates. The errors in $\langle R\rangle$, $\varphi^{\gamma'}$ and N_A were treated as sample standard-deviations from multiple independent measurements. Determination of the error in N_V was based on standard error propagation methods [37].

Vickers microhardness measurements were performed on polished samples using a Struers Duramin 5 microhardness tester, with an applied load of 1 kg for 5 s at ambient temperature. Flow-stress measurements were performed using a MTS 810 Material Test System. The cylindrical samples were deformed at a constant nominal strain-rate of 1×10^{-4} s^{-1} under an Ar atmosphere, with the sample temperature controlled within ±3 °C of the target temperature. Two compressive load-jump creep tests were performed in air at 850 ± 3 °C, with stresses ranging from 230 MPa to 345 MPa and from 344 MPa to 430 MPa, and total accumulated strains of 4.4% and 6.0%, respectively. Each load was maintained for a time sufficient to achieve stationary-state creep. Creep tests were terminated when the strain rate increased continuously under a constant stress, indicating sample failure.

3. Results and discussion

3.1. Microstructural evolution during aging

A SEM-EDS analysis of a bulk sample of Co–19.6Ni–7.6Al–7.4W–4.1Ti indicated that the sample was completely solutionized, as only a single γ(f.c.c.)-phase was observed and the sample appeared homogenous within the spatial resolution of EDS (~1 μm).

Back-scattered SEM micrographs of alloys aged at 900 °C from 4 h to 2000 h are displayed in Fig. 1 at the same magnification (40.0 k). The alloy exhibited a two-phase γ(f.c.c.)/$\gamma'(L1_2)$ microstructure through 2000 h with no precipitates of a third-phase present in the grains or at the grain boundaries (GBs), Fig. A1. For all aging conditions, the $\gamma'(L1_2)$-precipitates were aligned along ⟨100⟩-directions. After 4 h and 16 h of aging, the $\gamma'(L1_2)$-precipitates displayed visibly rounded-corners and were often interconnected into irregularly-shaped precipitates, caused by the coagulation and coalescence of neighboring $\gamma'(L1_2)$-precipitates. After 65 h of aging, the $\gamma'(L1_2)$-precipitates exhibited a cuboidal-like morphology, with flat {100} γ(f.c.c.)/$\gamma'(L1_2)$-heterophase-interfaces. Some of the $\gamma'(L1_2)$-precipitates were elongated with an aspect ratio greater than two. As aging time prolongs to 2000 h, the rounded {110} edges became somewhat sharper, which is consistent with study in Ni-based superalloys indicating that {110} interfaces have higher interfacial free energy than {100} interfaces [38]. These continous changes of morphology with aging time suggest the presence of an elastically induced spheroidal-to-cuboidal morphological transition, as was reported earlier in other γ(f.c.c.)/$\gamma'(L1_2)$-alloy-systems, e.g., Ni-based superalloys [39] and binary Co–Ti alloys [40]. Our observation that a sample aged for 1 h had spheroidal precipitates, Fig. A2, is in accordance with a TEM study of Meher et al. [41], and the phase-field model of Jokisaari et al. [42] for the Co–Al–W system. The latter articles indicate that $\gamma'(L1_2)$-precipitates exhibit a spheroidal morphology in the early-stages of an aging treatment. As aging proceeds, an increase in precipitate diameter makes the cuboidal morphology energetically more favorable, because the elastic strain energy associated with the $\gamma'(L1_2)$-precipitates dominates over the interfacial free energy [43–47].

3.2. Coarsening kinetics

The results of the stereological analyses of the $\gamma'(L1_2)$-precipitate microstructure are summarized in Table 1 and plotted in Fig. 2. Coarsening kinetics, for diffusion-limited coarsening, follow an LS-type coarsening-rate equation for $\langle R(t)\rangle$,

$$\langle R(t)\rangle^p - \langle R(t_0)\rangle^p = K(t - t_0) \tag{3}$$

where t is the aging time, t_0 is the aging time corresponding to the onset of the stationary coarsening state, p is the temporal exponent, and K is the associated coarsening rate constant. The LS-model was developed to describe a binary alloy, albeit without including any thermodynamics. Recently, Philippe and Voorhees (P–V), in the most general treatment to date, have demonstrated that the LS's coarsening temporal exponents are valid for multicomponent alloys with, however, different rate constants as the number of components in an alloy increases; e.g., ternary, quaternary, quinary, etc; see Eqs. (41) and (42) in Ref. [35]. For $\langle R(t)\rangle$ the temporal exponent p is equal to 1/3, with a rate constant, K, specifically for a quinary alloy [35]. Furthermore, according to the P–V model, the volumetric number density (number per unit volume) of precipitates, $N_V(t)$, in multinary alloys evolve as

$$N_V(t) \cong 0.21 \frac{\varphi_{eq}^{\gamma'}}{K} t^{-1} \tag{4}$$

where $\varphi_{eq}^{\gamma'}$ is the equilibrium volume fraction of the $\gamma'(L1_2)$-precipitate phase and the temporal exponent of $N_V(t)$, q, is equal to −1; note that K is the same K as in Eq. (3). The temporal evolution of the $\gamma'(L1_2)$-volume-fraction, $\varphi^{\gamma'}(t)$, is displayed in Fig. 2(a). In an absolutely pure stationary-state coarsening regime, the precipitate volume fraction should be equal to the equilibrium volume fraction of $\gamma'(L1_2)$-phase, which is a constant independent of time (t). Since the value of the $\gamma'(L1_2)$-volume-fraction at 4 h aging is significantly smaller than for the other data points, it is evident that at 4 h the system is not in a quasi-stationary-state coarsening regime and it was therefore excluded from the coarsening analyses.

Fig. 2(b) displays the temporal evolution of the precipitate circular-area-equivalent mean radius, $\langle R(t)\rangle$, from which the temporal exponent was determined to be $p = 3.49 \pm 0.18$ (coefficient of determination $\xi^2 = 0.99838$), employing a nonlinear multivariate regression analysis [48]. It is well known that a nonlinear multivariate regression analysis is a more accurate mathematical method to determine the temporal exponents of a nonlinear equation as opposed to performing a linear regression analysis with different values of the temporal exponents and to compare the coefficients of determination, ξ^2(see Fig. A3 of the present work, also Supplement A1 of [47]). Linearizing a non-linear equation by imposing on it a temporal exponent and then using what is a least squares-fit approach implies that one is asking how good the fit is compared to a straight line, which doesn't describe the experimental data. The value of the associated coarsening rate constant $K = 8.24 \times 10^{-31}$ m$^{3.49}$s^{-1} was determined from the same nonlinear multivariate regression analysis of $\langle R(t)\rangle$. Next, the coarsening rate constant was determined to be $K = 1.52 \times 10^{-27}$ m^3 s^{-1} ($\xi^2 = 0.99958$), using a linear regression analysis with p equal to 3; in this case the dimensions of K are correct.

Fig. 2(c) displays the temporal evolution of $N_V(t)$, from which

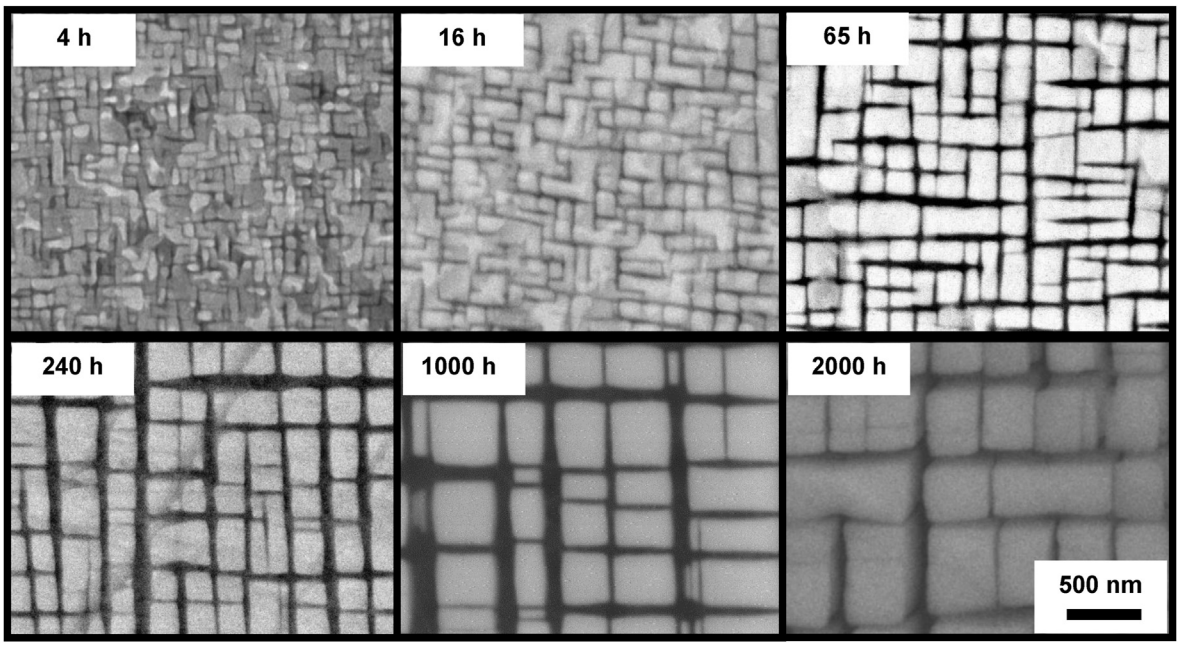


Fig. 1. Back-scattered SEM images of etched Co−19.6Ni−7.6Al−7.4W−4.1Ti specimens aged at 900 °C for 4 h, 16 h, 65 h, 240 h, 1000 h, and 2000 h. The dark contrast indicates the selectively-etched γ(f.c.c.)-matrix while the bright contrast indicates γ′($L1_2$)-precipitates.

Table 1
γ′($L1_2$)-precipitate-volume-fraction, $\varphi^{\gamma'}$, mean radius, $\langle R \rangle$, and number density, N_V, of a Co−19.6Ni−7.6Al−7.4W−4.1Ti at. % alloy after different aging times at 900 °C.

Aging Time, t (h)	Volume Fraction, $\varphi^{\gamma'}$ (%)	Mean Radius, $\langle R \rangle$ (nm)	Number Density, N_V (10^{18} m^{-3})
4	55 ± 3	27 ± 11	4300 ± 840
16	64 ± 3	60 ± 27	375 ± 35
64	61 ± 3	87 ± 26	108 ± 11
240	64.4 ± 2.5	119 ± 37	54.5 ± 5.1
1000	62.6 ± 2.2	178 ± 52	19.0 ± 2.3
2000	63.9 ± 1.5	224 ± 61	8.64 ± 1.01

the temporal exponent was determined to be $q = -0.74 \pm 0.04$ ($\xi^2 = 0.97102$), obtained using a nonlinear multivariate regression analysis. The value of the associated coarsening rate constant $K = 1.12 \times 10^{-25}$ m^3 s$^{-0.74}$ was determined from the same nonlinear multivariate regression analysis of $N_V(t)$. Furthermore, the P−V model predicts the coarsening rate constant to be $K = 3.97 \times 10^{-27}$ m^3 s^{-1} ($\xi^2 = 0.81198$), utilizing a linear regression analysis, with the temporal exponent of $N_V(t)$, q, set equal to −1; the rate constant has the correct dimensions. It is experimentally difficult to obtain $q = -1$ for $N_V(t)$ as it is continuously decreasing inversely, with increasing aging time; which is the case for a system where coarsening is controlled by the coagulation-coalescence mechanism but it is not the case for the classical evaporation-condensation mechanism for coarsening. For the evaporation-condensation mechanism the edge-to-edge distance between precipitates is continuously increasing. And concomitantly the root-mean-square (RMS) diffusion distances among the γ′($L1_2$)-precipitates are increasing parabolically with aging time. Specifically, the RMS diffusion distance is proportional to the square-root of the diffusivity of the solute atoms in the matrix times the aging time (t). In contrast, Plotnikov et al. investigated a Ni-12.5 at.% Al alloy aged at 823 K (550 °C) and concluded that the edge-to-edge distance between precipitates was at first large (~100 nm) but with increasing aging time it decreased to a small value (~5 nm) for a period of ~1 h−64 h and then it increased again with increasing aging time, until it reached a value of ~37.4 nm at 4096 h; see Fig. 8(b) in Ref. [47], whose behavior was completely different from that of the evaporation-condensation mechanism, where the edge-to-edge distance between precipitates is always increasing with increasing aging time. Thus, Eq. (4) is not applicable when the coagulation-coalescence mechanism is operative. To obtain $q = -1$ it is necessary to age at a given temperature for a very long aging time [49,50], when the evaporation-condensation mechanism dominates. In conclusion, because we know the coarsening mechanism for our alloy is the coagulation-coalescence mechanism we don't put too much stock in the value of K we calculated for $N_V(t)$.

Assuming coarsening is controlled by bulk diffusion, the temporal exponents are $p = 3$ and $q = -1$ as derived from the LS and P−V models for the evaporation-condensation mechanism. Alternatively, Wagner [34], Marqusee and Ross [51] derived $p = 2$ assuming the kinetics are controlled by the inability of an interface to act as a perfect sink for solute atoms, which means that there isn't a concentration gradient of the solute atoms in the matrix, γ(f.c.c.). An absolutely imperfect sink implies $p = 2$, while it may be possible to have an imperfect sink for which p lies between 2 and 3. Our experimental measurement of p (= 3.49 ± 0.18) suggests that diffusion-controlled kinetics are dominating, rather than interface-controlled kinetics (as interface-controlled kinetics imply $p < 3$). The measured values of p (= 3.49 ± 0.18) and q (= −0.74 ± 0.04) deviate from the LS and P−V models, where $p = 3$ and $q = -1$. Similar results have been observed in other Co-based superalloys [16,17,52]. Deviation from a stationary-prediction of N_V has been reported in Ni-based superalloys [39]. The discrepancy between the present experimental results and the LS values for diffusion-controlled coarsening indicates that a true stationary-state has most likely not been achieved and hence the system was still in a quasi-stationary state, where the volume fraction is asymptotically approaching a constant value. We also note that transient coarsening lasts longer in systems with a large precipitate volume-fraction (more than 50% as shown by Ref. [53]), where a stationary-state is rarely achieved.

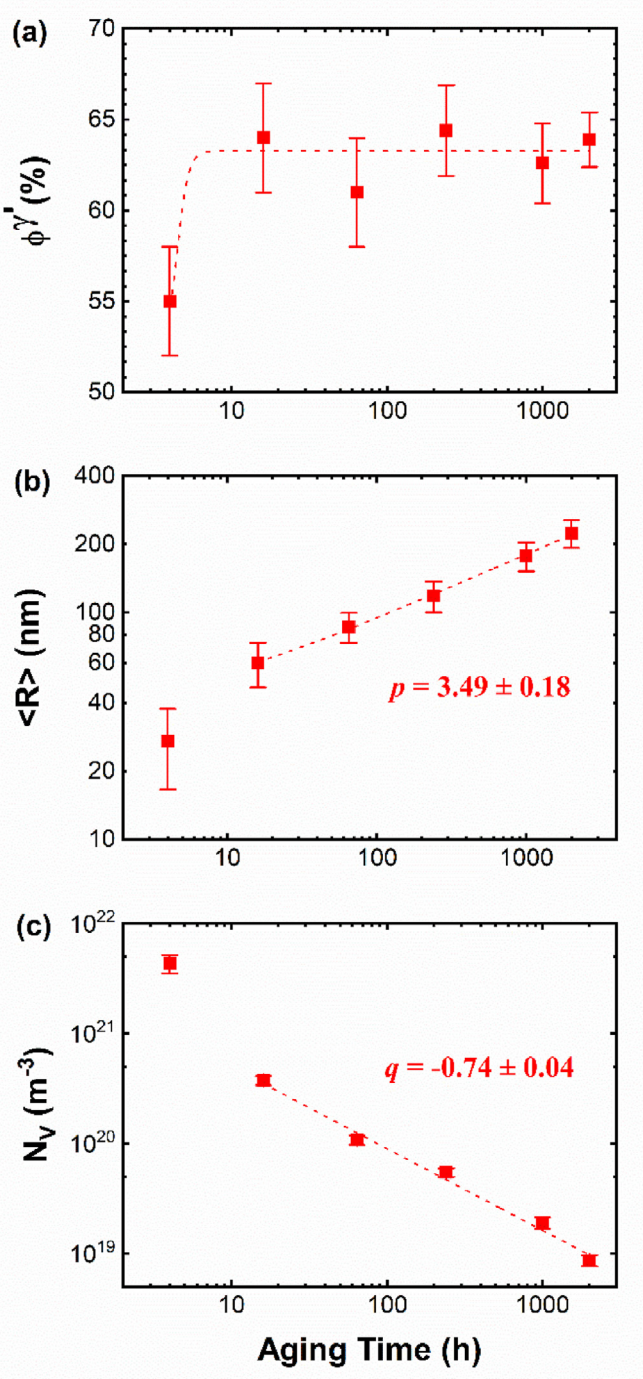


Fig. 2. Temporal evolution of $\gamma'(L1_2)$-precipitates: (a) volume fraction; (b) mean radius; and (c) number density in the Co−19.6Ni−7.6Al−7.4W−4.1Ti alloy aged at 900 °C through 2000 h (83 days).

3.3. Mechanical behavior

As demonstrated in Fig. 3, the Vickers microhardness of the alloy increased continuously from 0 to 4 h, and achieved a nearly flat plateau at 8 h with a weak peak of 3.80 ± 0.10 GPa at 240 h. Beyond 240 h, the microhardness decreased slightly, with a value of 3.58 ± 0.11 GPa at the longest measured aging time of 2000 h. The microhardness of Co−19.6Ni−7.6Al−7.4W−4.1Ti alloy in this work is comparable to that of a Co−10.3Ni−7.0W−6.3Al−4.1Ti alloy, aged at the same temperature, with a similar $\gamma'(L1_2)$-volume-fraction

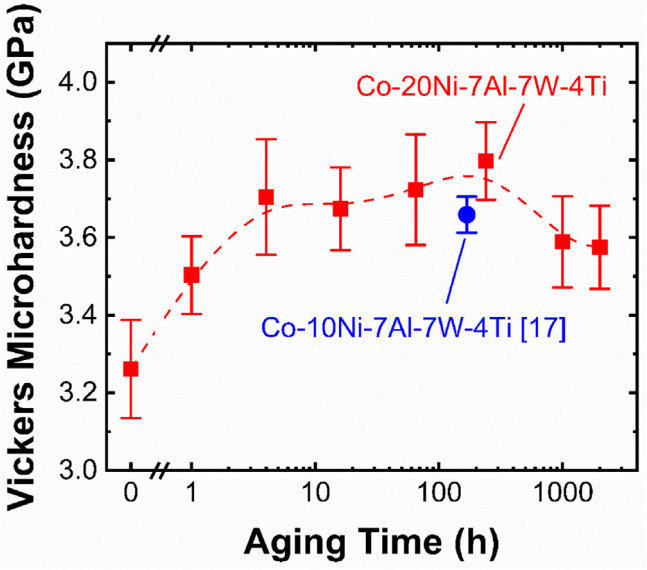


Fig. 3. Room temperature Vickers microhardness measurements of the Co−19.6Ni−7.6Al−7.4W−4.1Ti alloy (red squares) after aging at 900 °C for 0, 1, 4, 16, 64, 240, 1000, 2000 h and the Co−10.3Ni−7.0W−6.3Al−4.1Ti alloy (blue circle) after aging at 900 °C for 168 h, from Ref. [17]. (For interpretation of the references to colour in this figure legend, the reader is referred to the Web version of this article.)

[17]. Since the $\gamma'(L1_2)$-volume-fraction $\varphi^{\gamma'}$ is stable after 16 h, an optimal $\gamma'(L1_2)$ mean-radius for precipitate strengthening, $\langle R \rangle = 119 \pm 37$ nm, is achieved at 240 h of aging; this peak-aged condition is used for the flow-stress and creep measurements, read below.

Although the microhardness test has been widely applied, interpretation of Vickers microhardness values, in terms of a physical model, remains challenging due to the complexity of the microstructures and the mechanical analyses. For example, the development of fine secondary $\gamma'(L1_2)$-nanoprecipitates due to quenching after aging may influence the Vickers microhardness measurements at room temperature [54,55]. Nevertheless, an empirical linear relationship between Vickers microhardness and the 0.2% flow-stress has been proposed for superalloys [56]. At early aging times, the initial increase in microhardness is the result of an increase in the mean precipitate radius [57]. An increase in the $\gamma'(L1_2)$-volume-fraction is also a contributing factor before 16 h. After 240 h, the rapid decrease in the $N_V(t)$ of $\gamma'(L1_2)$-precipitates causes a diminishment of precipitate strengthening. These two factors compensate one another to form a plateau. We appreciate the fact that more advanced techniques and more rigorous quantitative analyses are needed to confirm this explanation.

Fig. 4 shows the results of 0.2% flow stress measurements from the archival literature for other superalloys, included for comparative purposes. In the present alloy (Co−20Ni−7Al−7W−4Ti), the peak flow stress reached ~705 MPa at 750 °C, a significant improvement compared to an alloy with 10 at.% less in Ni concentration (Co−10Ni−7Al−7W−4Ti), with a peak flow stress of ~675 MPa at 750 °C [17]. For the Co−9Al−9W ternary alloy [3] without any Ni or Ti addition, the peak-stress was at ~700 °C with a value of ~460 MPa. All the alloys exhibited an anomalous increase in flow-stress above 600 °C, where the addition of Ni and Ti increased the flow stress, and shifted the peak stress toward a higher temperature. Addition of 10−20 at.% Ni and 4 at.% Ti suppressed the formation of Ti-containing topological closed-packed (TCP phases), yielding a larger $\gamma'(L1_2)$-volume-fraction (~62% at 900 °C for Co−10Ni−7Al−7W−4Ti [17], ~64% at 900 °C for

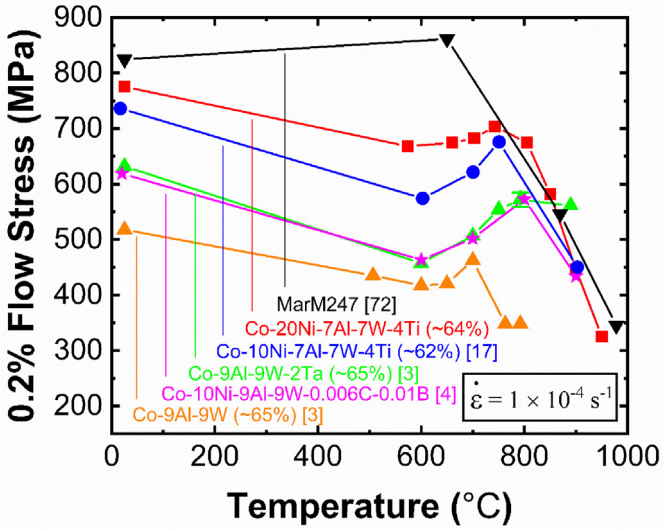


Fig. 4. Temperature dependence of the 0.2% flow stress for the Co−19.6Ni−7.6Al−7.4W−4.1Ti alloy (red data points, labeled Co−20Ni−7Al−7W−4Ni) aged at 900 °C for 240 h. Also plotted are archival literature values of the 0.2% flow stress for other Co-based superalloys with a similar $\gamma'(L1_2)$-volume-fraction (numbers in brackets indicate the percentage) as well as the commercial Ni-based superalloy MarM247. Data points for Co−9Al−9W and Co−9Al−9W−2Ta are taken from Ref. [3], data for the Co−10Ni−9Al−9W−0.006C−0.01B, Co−10Ni−7Al−7W−4Ti and MarM247 alloys are adapted from Refs. [4,17,72], respectively. All the data are measured by compressive tests at a strain rate of $1 \times 10^{-4}\ s^{-1}$. The error bars are negligible on the present scale. (For interpretation of the references to colour in this figure legend, the reader is referred to the Web version of this article.)

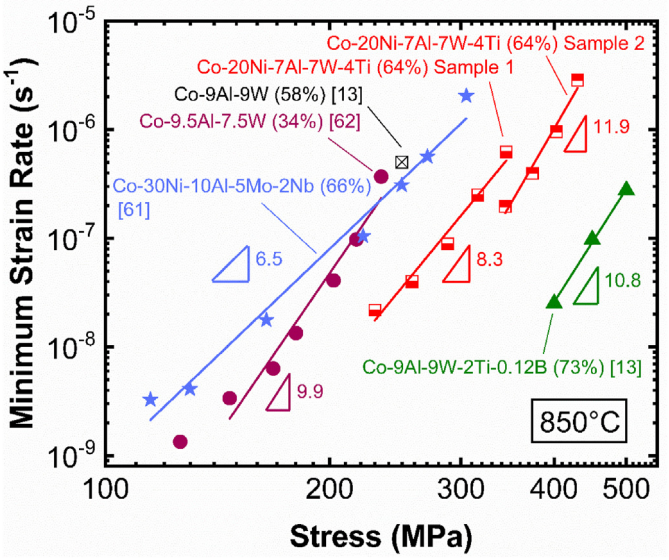


Fig. 5. Norton plots of minimum strain rate vs. stress at 850 °C for the present alloy (labeled Co−20Ni−7Al−7W−4Ni) aged at 900 °C for 240 h, as well as literature data for other Co-based superalloys. Data for the Co−9Al−9W−2Ti−0.12B and Co−9Al−9W alloys are adapted from Ref. [13], while the data for the Co−30Ni−10Al−5Mo−2Nb and Co−9.5Al−7.5W alloys are taken from Refs. [61,62], respectively. The $\gamma'(L1_2)$-volume-fraction (in %, in parentheses) and the apparent stress exponent n are noted for each alloy.

Co−20Ni−7Al−7W−4Ti). It is noted that Shi et al. [18] performed flow-stress measurements from tensile tests in an alloy with a similar composition (Co−17Ni−9Al−5W−3Ti), and their measurements of flow-stress followed the same temperature dependence as in our study, albeit ~100 MPa lower in the entire temperature range. The difference in the flow-stress measurement between Shi et al. and the present study suggests the presence of a tension-compression asymmetry, although the differences in compositions may also contribute to the discrepancy (discussed below). Hence, only the flow-stress measurements from the compressive tests at the same strain rate ($1 \times 10^{-4}\ s^{-1}$) are directly compared in Fig. 4.

Theoretical interpretations of flow-stress measurements are challenging because deformation mechanisms in Co-based superalloys are not fully understood. Prior research has shown that the addition of Ni and Ti increases the superlattice intrinsic stacking fault (SISF)- and the complex stacking fault (CSF)-energies [4,58]. There is also evidence suggesting that deformation through anti-phase boundaries (APBs) is the active mechanism in some Co−Ni-based superalloys [59]. Further investigations are needed to identify whether the SISF mechanism is the dominant deformation mechanism (as in Co−Al−W-based alloys) after adding 20 at.% Ni to this superalloy.

Creep data for Co−19.6Ni−7.6Al−7.4W−4.1Ti alloy are plotted in Fig. 5. The apparent stress exponent n was determined from the simple Norton power law for secondary-creep at constant temperature

$$\dot{\varepsilon} = A\sigma^n \tag{5}$$

where $\dot{\varepsilon}$ is the minimum strain rate, A is the pre-exponential factor, σ is the applied stress, and n is the apparent stress exponent. Both samples investigated herein displayed apparent stress exponents ($n \approx 10$) similar to other Co−Al−W-based superalloys. These relatively large values of n suggest a mechanism related not only to dislocation-interactions with precipitates, but also to grain-boundary (GB) weakening [13,60]. Sample 1 was crept for about 200 h before failure at 4.4% strain. Sample 2 was crept for about 24 h before failure at 6.0% strain. Both samples failed by GB decohesion. The intergranular failure-mode in compression has been observed previously in Co-based superalloys [13,61] and can be avoided by microalloying with elements such as B and Zr, which strengthen GBs [62,63]. Furthermore, a small concentration of B is present in the grain interiors, which partitions into the $\gamma'(L1_2)$-phase [63] and it also may strengthen the precipitates. The creep strength of the alloy investigated herein exceeds significantly that of the ternary Co−Al−W alloy [62], as well as the tungsten-free Co−30Ni−10Al−5Mo−2Nb alloy [61]. It is, however, apparent that the B-containing Co−9Al−9W−2Ti−0.12B alloy is significantly more creep-resistant [13], confirming boron's GB strengthening effect.

The discrepancy in strain rate between samples 1 and 2 (about a factor of 3 at 345 MPa) may be related to rafting. Post-crept SEM results (Section 3.4) demonstrate that a number of grains in sample 1 contain rafted precipitates. In contrast, no rafting was observed in sample 2. It has been suggested [32] that rafting facilitates creep when dislocations cut through precipitates (that is, low temperatures and high stresses), whereas rafting inhibits creep when dislocations climb over precipitates (that is, high temperatures and low stresses). Previous observations have suggested that precipitate shearing is the main deformation mechanism up to 900 °C in Co-based superalloys [59,64,65]. Thus, the higher strain-rate of sample 1 at 345 MPa is consistent with its rafted microstructure as compared to the unrafted sample 2 with a slower creep-rate. The loss of coherency during rafting [27] can be detrimental to strength [66]. Other differences between samples 1 and 2, including topology of the grain structure (e.g., diameter, morphology, orientation, etc.) and the spatial distribution of different grains, may also change the load distribution and the load transfer among grains. Since the grain diameter is relatively large in both samples (several hundred μm), the variation of grain-structure between the two samples is non-negligible and may explain some of the observed discrepancies in creep behavior.

3.4. Post-crept microstructure

Although rafting has been studied extensively in single-crystal superalloys [26,32], less is known about the rafting behavior of polycrystalline superalloys. The precipitate morphology and rafted microstructure of post-crept sample 1 are displayed in Fig. 6. The samples in Fig. 6(a, c) were imaged on a cross-section perpendicular to the applied stress, while those in Fig. 6(b, d) were imaged on a cross-section parallel to the applied stress.

As displayed in Fig. 6(a, b), the $\gamma'(L1_2)$-precipitates remain cuboidal and exhibit sharp edges in the unrafted grains. While the centers of the grains remain unrafted, the regions neighboring the GBs may be rafted due to local stress concentrations near GBs, Fig. A4. The widths of these rafted regions are typically a few micrometers. Because the compressive stress is perpendicular to the GB, the rafted $\gamma'(L1_2)$-precipitates are aligned parallel to the GB.

In fully rafted-grains, there are $\gamma'(L1_2)$-rafts normal to the loading axis (N-type), Fig. 6(c, d). The rafted γ' $(L1_2)$-precipitates have a plate-like morphology, similar to those observed in Ni-based superalloys subjected to a tensile-stress [54,67]. In this case, the γ(f.c.c.)/$\gamma'(L1_2)$-heterophase-interfaces are no longer flat but rather exhibit a complex, wavy topology, possibly as a result of relief from the misfit elastic stresses. Furthermore, the $\gamma'(L1_2)$-rafts appear interconnected with one another, giving rise to an interpenetrating γ(f.c.c.)/$\gamma'(L1_2)$ architecture. It is also possible that $\gamma'(L1_2)$-phase is continuous, while the γ(f.c.c.)-phase is not: this so-called topological inversion has been observed during the last stage of creep in Ni-based superalloys [67]. The average thickness of the $\gamma'(L1_2)$-plates in one fully rafted grain in sample 1 is 175 ± 7 nm, with an increase in the $\gamma'(L1_2)$-volume-fraction to 79.4 ± 1.3%, from 64.4 ± 2.5% in the pre-crept condition. This increase in the $\gamma'(L1_2)$-volume-fraction may be the consequence of a larger equilibrium $\gamma'(L1_2)$-volume-fraction at the creep temperature (850 °C) than at the aging temperature (900 °C). Using the PANDAT™ cobalt thermodynamic database [68,69] from CompuTherm, the equilibrium $\gamma'(L1_2)$-volume-fraction is predicted to be 65% at 850 °C compared to 61% at 900 °C. Alternatively, Thermo-calc using the TCNI8 thermodynamic database [70,71] predicts an equilibrium $\gamma'(L1_2)$-volume-fraction of 76% at 850 °C compared to 64% at 900 °C. Both databases thus predict an increase in the $\gamma'(L1_2)$-volume-fraction (by 4 and 12%, respectively), when the temperature is reduced from 900 to 850 °C, which is in approximate agreement with the observed value of 15%. Thus, it is likely that additional precipitate growth occurs during creep, which leads to an increase in the $\gamma'(L1_2)$-volume-fraction. This occurs slowly because the matrix is solute-poor after the previous aging treatment and concurrently with rafting occurring in some of the grains, without any noticeable changes in the creep curves.

4. Summary and conclusions

This study involves an investigation of the precipitate morphology, coarsening kinetics, microhardness, flow-stress, creep, and rafting of a polycrystalline Co−19.6Ni−7.6Al −7.4W−4.1Ti at.% superalloy aged at 900 °C for different aging times up to 2000 h. The analyses produced the following results:

- There are only two phases present up to 2000 h of aging; the γ(f.c.c.)-matrix and $\gamma'(L1_2)$-precipitates, Fig. 1. Coarsening is occurring via the coagulation-coalescence mechanism as opposed to the evaporation-condensation ("the big precipitates eat the small precipitates").
- The $\gamma'(L1_2)$-volume-fraction reaches a value of 64% after 16 h of aging at 900 °C, Fig. 2. The peak-aged circular-area-equivalent mean-radius of the $\gamma'(L1_2)$-precipitates is 119 ± 37 nm. A nonlinear multivariate regression analysis yields a temporal exponent of $p = 3.49 \pm 0.18$ for the equivalent radius, and $q = -0.74 \pm 0.04$ for the volumetric number density. These results suggest that the system is undergoing quasi-stationary coarsening, where the volume fraction is asymptotically approaching a constant but has yet to achieve its equilibrium value at 2000 h.

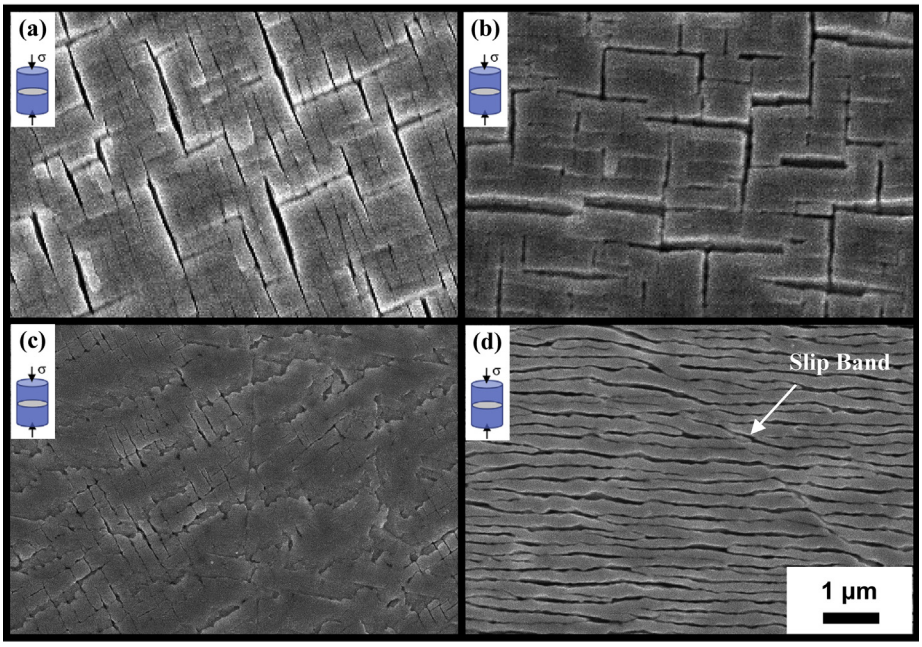


Fig. 6. SEM micrographs of the post-crept microstructure of sample 1. The imaged cross-section was perpendicular to the loading direction in (a) and (c), and parallel to the loading direction in (b) and (d). The $\gamma'(L1_2)$-precipitates remained cuboidal in some grains, as displayed in (a) and (b), while in other grains the $\gamma'(L1_2)$-precipitates were rafted, (c) and (d). Slip bands were observed in the rafted grain, indicated in (d) by an arrow.

- The Philippe-Voorhees (P–V) equation for the number density, $N_V(t)$, of precipitates is invalid when coarsening occurs through a coagulation-coalescence mechanism because the mean edge-to-edge distances among precipitates first decreases to a small value, and then remains constant for a long period of time and finally commences increasing.
- The Vickers microhardness values achieve a nearly flat-plateau at 4 h, with a small peak of 3.80 ± 0.10 GPa at 240 h, Fig. 3. The peak anomalous flow-stress value is 705 MPa at 750 °C, which confirms the strengthening effect produced by additions of Ni and Ti to the ternary Co–Al–W composition for this quinary alloy, Fig. 4.
- The creep resistance exceeds that of the ternary Co–Al–W alloy, but is smaller than that of the quaternary Co–Al–W–Ti alloy with a B addition for grain-boundary strengthening, Fig. 5. N-type rafting (plate-like precipitates normal to the loading axis) is observed in several grains after compressive-creep experiments, Fig. 6. A partially-rafted sample displays less creep resistance than a fully unrafted sample. The $\gamma'(L1_2)$-volume-fraction increased from 64 to 79% after creep, as a result of additional precipitate-growth during creep.

CRediT authorship contribution statement

Chunan Li: Conceptualization, Validation, Formal analysis, Investigation, Data curation, Writing - original draft, Visualization. **Ding-Wen Chung:** Conceptualization, Software, Validation, Investigation, Resources, Data curation, Writing - review & editing. **David C. Dunand:** Conceptualization, Methodology, Resources, Writing - review & editing, Supervision, Project administration, Funding acquisition. **David N. Seidman:** Conceptualization, Methodology, Formal analysis, Writing - review & editing, Supervision, Project administration, Funding acquisition.

Declaration of competing interest

The authors declare that they have no known competing financial interests or personal relationships that could have appeared to influence the work reported in this paper.

Acknowledgements

This work was performed with financial assistance award number 70NANB14H012 from U.S. Department of Commerce, National Institute of Standards and Technology, as part of the Center for Hierarchical Materials Design at Northwestern University. SEM studies were performed at the Electron Probe Instrumentation Center (EPIC) facility of the Northwestern University Atomic and Nanoscale Characterization Experimental Center (NUANCE), supported by the Soft and Hybrid Nanotechnology Experimental (SHyNE) Resource (NSF ECCS-1542205); the Northwestern University Materials Research Science and Engineering Center (NU-MRSEC) program (NSF DMR-1121262); the International Institute for Nanotechnology (IIN); and the State of Illinois, through the IIN. This research made use of the following facilities that receive support from the NU-MRSEC Program (NSF DMR-1121262): The Materials Characterization and Imaging Facility (MatCI) and the Central Laboratory for Materials Mechanical Properties (CLaMMP). We also gratefully thank Dr. Hyeji Park (Kookmin University) for assistance with obtaining SEM images, Dr. Anthony De Luca (Northwestern University) for discussion concerning creep-testing, and Dr. Eric A. Lass (NIST) for assistance with thermodynamic calculations.

Appendix

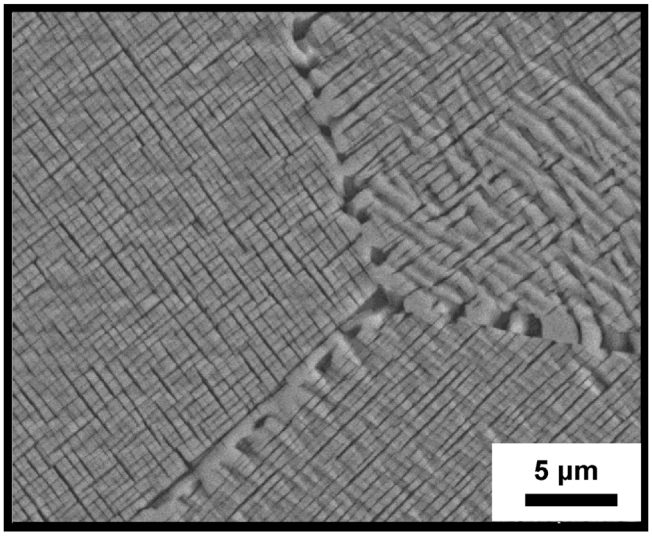


Fig. A1. Back-scattered SEM micrograph of a triple junction in a 2000 h-aged sample. This γ(f.c.c.)/$\gamma'(L1_2)$-structure displays coarsened $\gamma'(L1_2)$-precipitates at the grain boundaries but no other phases were observed.

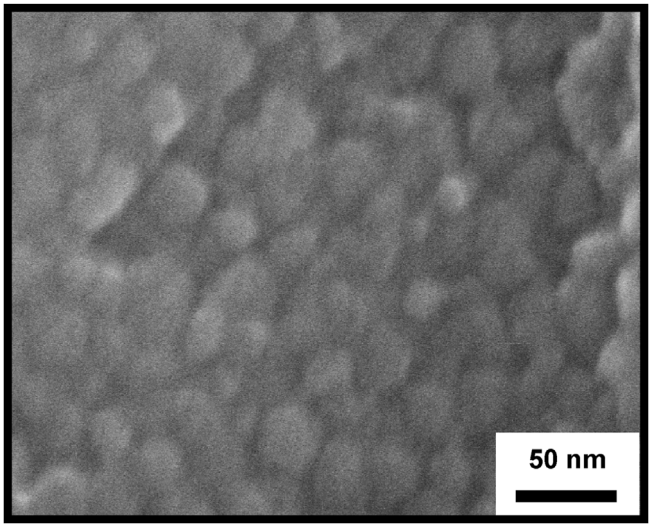


Fig. A2. Secondary-electron scanning electron microscope (SEM) micrograph of a sample aged at 900 °C for 1 h. The $\gamma'(L1_2)$-precipitates have an approximately spheroidal morphology with a diameter of 10–20 nm. Because of the limited spatial resolution of the SEM, the precipitate diameter and volume-fraction were not determined.

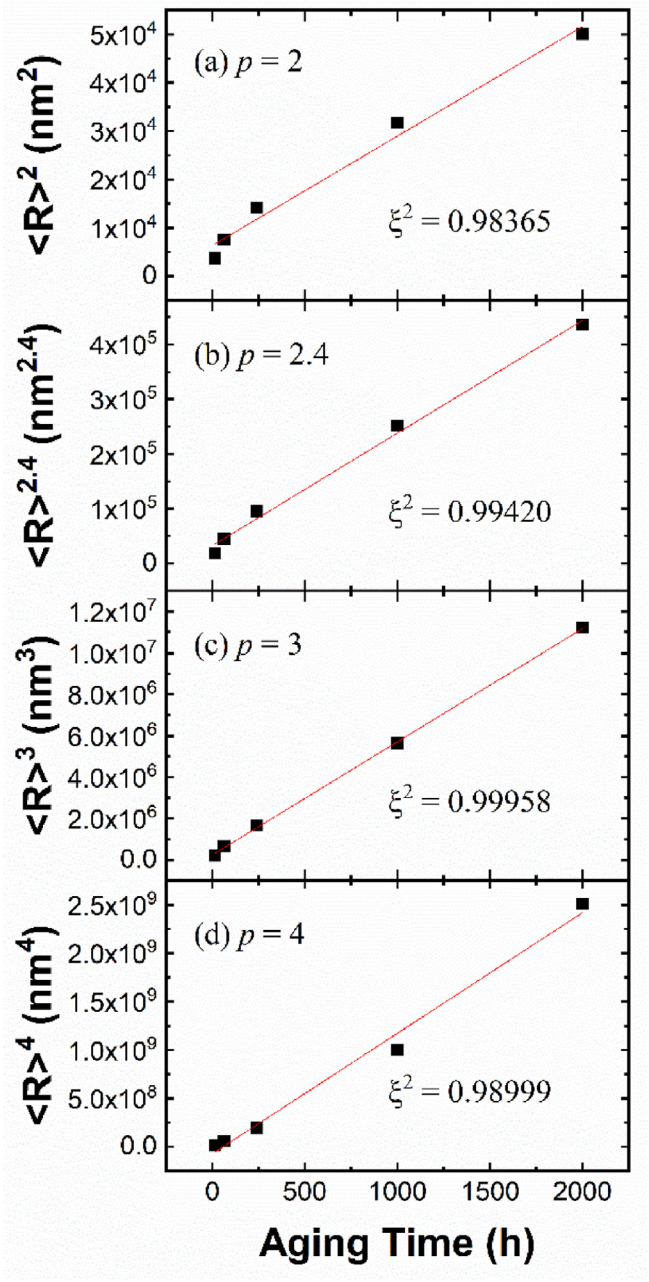


Fig. A3. Linear regression analyses for $\langle R(t) \rangle^p$ versus aging time at 900 °C for: (a) $p = 2$; (b) $p = 2.4$; (c) $p = 3$; and (d) $p = 4$. The goodness-of-fit to a straight line is measured by the coefficient of determination, ξ^2, given in each plot. Note that the ξ^2 values for all the p values between 2 and 4 are close to 1 (>0.98). Therefore, ξ^2 values from these linear regression analyses for $\langle R(t) \rangle^p$ versus time are very insensitive to changes in p in the range 2–4.

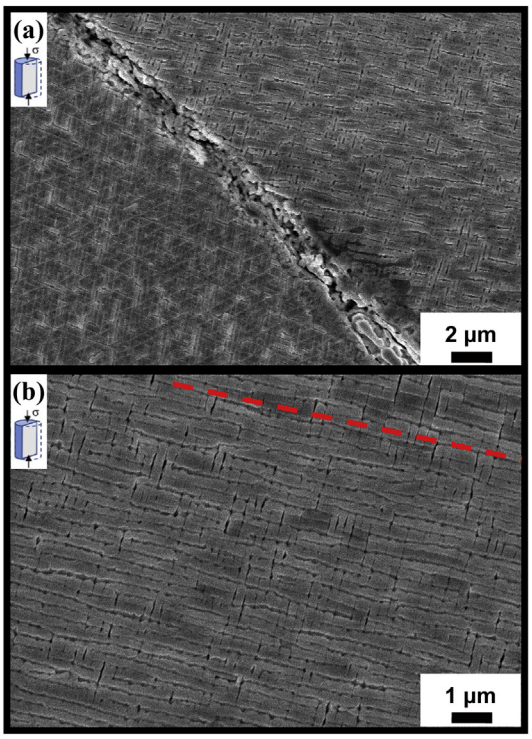


Fig. A4. Back-scattered SEM micrographs of a rafted-region abutting a grain-boundary in a partially-rafted grain of post-crept sample 1. (a) The grain boundary is oxidized and cracked. In the top-right corner there is a rafted region. (b) A rafted region in the upper top-right direction next to (a), where the red dashed line indicates the boundary between the rafted and unrafted regions. The unrafted region has a microstructure similar to Fig. 6(b) with a flat γ(f.c.c.)/γ′($L1_2$) interface instead of the modulated γ(f.c.c.)/γ′($L1_2$) interfaces in the rafted regions. The imaged cross-section is parallel to the loading direction, as indicated by the inset figure.

References

[1] J. Sato, T. Omori, K. Oikawa, I. Ohnuma, R. Kainuma, K. Ishida, Cobalt-base high-temperature alloys, Science 312 (2006) 90–91.
[2] C.S. Lee, Precipitation-hardening Characteristics of Ternary Cobalt-Aluminum-X Alloys, University of Arizona, Tucson, 1971.
[3] A. Suzuki, G.C. DeNolf, T.M. Pollock, Flow stress anomalies in γ/γ′ two-phase Co–Al–W-base alloys, Scripta Mater. 56 (2007) 385–388.
[4] A. Suzuki, H. Inui, T.M. Pollock, $L1_2$-strengthened cobalt-base superalloys, Annu. Rev. Mater. Res. 45 (2015) 345–368.
[5] S. Neumeier, H.U. Rehman, J. Neuner, C.H. Zenk, S. Michel, S. Schuwalow, J. Rogal, R. Drautz, M. Göken, Diffusion of solutes in fcc Cobalt investigated by diffusion couples and first principles kinetic Monte Carlo, Acta Mater. 106 (2016) 304–312.
[6] M. Tsunekane, A. Suzuki, T.M. Pollock, Single-crystal solidification of new Co–Al–W-base alloys, Intermetallics 19 (2011) 636–643.
[7] J.E. Saal, C. Wolverton, Thermodynamic stability of Co–Al–W $L1_2$ γ′, Acta Mater. 61 (2013) 2330–2338.
[8] S. Kobayashi, Y. Tsukamoto, T. Takasugi, H. Chinen, T. Omori, K. Ishida, S. Zaefferer, Determination of phase equilibria in the Co-rich Co–Al–W ternary system with a diffusion-couple technique, Intermetallics 17 (2009) 1085–1089.
[9] E.A. Lass, R.D. Grist, M.E. Williams, Phase equilibria and microstructural evolution in ternary Co-Al-W between 750 and 1100 °C, J. Phase Equilibria Diffus. 37 (2016) 387–401.
[10] F. Xue, H.J. Zhou, X.F. Ding, M.L. Wang, Q. Feng, Improved high temperature γ′ stability of Co–Al–W-base alloys containing Ti and Ta, Mater. Lett. 112 (2013) 215–218.
[11] K. Shinagawa, T. Omori, J. Sato, K. Oikawa, I. Ohnuma, R. Kainuma, K. Ishida, Phase equilibria and microstructure on γ′ phase in Co-Ni-Al-W system, Mater. Trans. 49 (2008) 1474–1479.
[12] I. Povstugar, C.H. Zenk, R. Li, P.P. Choi, S. Neumeier, O. Dolotko, M. Hoelzel,

M. Göken, D. Raabe, Elemental partitioning, lattice misfit and creep behaviour of Cr containing γ′ strengthened Co base superalloys, Mater. Sci. Technol. 32 (2016) 220–225.
[13] A. Bauer, S. Neumeier, F. Pyczak, R.F. Singer, M. Göken, Creep properties of different γ′-strengthened Co-base superalloys, Mater. Sci. Eng. A 550 (2012) 333–341.
[14] M. Ooshima, K. Tanaka, N.L. Okamoto, K. Kishida, H. Inui, Effects of quaternary alloying elements on the γ′ solvus temperature of Co–Al–W based alloys with fcc/$L1_2$ two-phase microstructures, J. Alloys Compd. 508 (2010) 71–78.
[15] Y.W. Cui, M. Jiang, I. Ohnuma, K. Oikawa, R. Kainuma, K. Ishida, Computational study of atomic mobility for fcc phase of Co-Fe and Co-Ni binaries, J. Phase Equilibria Diffus. 29 (2007) 2–10.
[16] V.A. Vorontsov, J.S. Barnard, K.M. Rahman, H.Y. Yan, P.A. Midgley, D. Dye, Coarsening behaviour and interfacial structure of γ′ precipitates in Co-Al-W based superalloys, Acta Mater. 120 (2016) 14–23.
[17] P.J. Bocchini, C.K. Sudbrack, R.D. Noebe, D.C. Dunand, D.N. Seidman, Effects of titanium substitutions for aluminum and tungsten in Co-10Ni-9Al-9W (at%) superalloys, Mater. Sci. Eng. A 705 (2017) 122–132.
[18] L. Shi, J.J. Yu, C.Y. Cui, X.F. Sun, Microstructural stability and tensile properties of a Ti-containing single-crystal Co–Ni–Al–W-base alloy, Mater. Sci. Eng. A 646 (2015) 45–51.
[19] R.C. Reed, The Superalloys: Fundamentals and Applications, Cambridge University Press, Cambridge, 2008.
[20] T.M. Pollock, S. Tin, Nickel-based superalloys for advanced turbine engines: chemistry, microstructure, and properties, J. Propul. Power 22 (2006) 361–374.
[21] D.-W. Chung, D.S. Ng, D.C. Dunand, Influence of γ′-raft orientation on creep resistance of monocrystalline Co-based superalloys, Materialia 12 (2020).
[22] D.-W. Chung, J.P. Toinin, E.A. Lass, D.N. Seidman, D.C. Dunand, Effects of Cr on the properties of multicomponent cobalt-based superalloys with ultra high γ' volume fraction, J. Alloys Compd. (2020) 832.
[23] D.S. Ng, D.-W. Chung, J.P. Toinin, D.N. Seidman, D.C. Dunand, E.A. Lass, Effect of Cr additions on a γ-γ' microstructure and creep behavior of a Co-based superalloy with low W content, Mater. Sci. Eng. A 778 (2020) 139108.
[24] D.J. Sauza, D.C. Dunand, D.N. Seidman, Microstructural evolution and high-temperature strength of a γ(f.c.c.)/γ'(L12) Co–Al–W–Ti–B superalloy, Acta Mater. 174 (2019) 427–438.
[25] F. Pyczak, A. Bauer, M. Göken, U. Lorenz, S. Neumeier, M. Oehring, J. Paul, N. Schell, A. Schreyer, A. Stark, F. Symanzik, The effect of tungsten content on the properties of $L1_2$-hardened Co–Al–W alloys, J. Alloys Compd. 632 (2015) 110–115.
[26] J. Coakley, E.A. Lass, D. Ma, M. Frost, D.N. Seidman, D.C. Dunand, H.J. Stone, Rafting and elastoplastic deformation of superalloys studied by neutron diffraction, Scripta Mater. 134 (2017) 110–114.
[27] J. Coakley, E.A. Lass, D. Ma, M. Frost, H.J. Stone, D.N. Seidman, D.C. Dunand, Lattice parameter misfit evolution during creep of a cobalt-based superalloy single crystal with cuboidal and rafted gamma-prime microstructures, Acta Mater. 136 (2017) 118–125.
[28] H. Mughrabi, The importance of sign and magnitude of γ/γ′ lattice misfit in superalloys—with special reference to the new γ′-hardened cobalt-base superalloys, Acta Mater. 81 (2014) 21–29.
[29] S. Socrate, D. Parks, Numerical determination of the elastic driving force for directional coarsening in Ni-superalloys, Acta Metall. Mater. 41 (1993) 2185–2209.
[30] S.G. Tian, C.R. Chen, J.H. Zhang, H.C. Yang, X. Wu, Y.B. Xu, Z.Q. Hu, Evolution and analysis of γ′ rafting during creep of single crystal nickel base superalloy, Mater. Sci. Technol. 17 (2001) 736–744.
[31] F. Pyczak, A. Bauer, M. Göken, S. Neumeier, U. Lorenz, M. Oehring, N. Schell, A. Schreyer, A. Stark, F. Symanzik, Plastic deformation mechanisms in a crept $L1_2$ hardened Co-base superalloy, Mater. Sci. Eng. A 571 (2013) 13–18.
[32] F.R.N. Nabarro, Rafting in superalloys, Metall. Mater. Trans. 27 (1996) 513–530.
[33] I.M. Lifshitz, V.V. Slyozov, The kinetics of precipitation from supersaturated solid solutions, J. Phys. Chem. Solids 19 (1961) 35–50.
[34] C. Wagner, Theorie der Alterung von Niederschlägen durch Umlösen (Ostwald-Reifung), Z. Elektrochem. 65 (1961) 581–591.
[35] T. Philippe, P.W. Voorhees, Ostwald ripening in multicomponent alloys, Acta Mater. 61 (2013) 4237–4244.
[36] J.C. Russ, R.T. Dehoff, Practical Stereology, second ed., Springer Science & Business Media, New York, 2012.
[37] L.G. Parratt, Probability and Experimental Errors in Science: an Elementary Survey, John Wiley, New York, 1961.
[38] Z. Mao, C. Booth-Morrison, C.K. Sudbrack, R.D. Noebe, D.N. Seidman, Interfacial free energies, nucleation, and precipitate morphologies in Ni-Al-Cr alloys: calculations and atom-probe tomographic experiments, Acta Mater. 166 (2019) 702–714.
[39] C.K. Sudbrack, T.D. Ziebell, R.D. Noebe, D.N. Seidman, Effects of a tungsten addition on the morphological evolution, spatial correlations and temporal evolution of a model Ni–Al–Cr superalloy, Acta Mater. 56 (2008) 448–463.
[40] C. Wang, J. Huang, H. Kong, Y. Lu, X. Liu, The effect of temperature and misfit on γ′ precipitation in Co-Ti alloys: phase-field modeling and experiments, J. Phase Equilibria Diffus. 41 (2020) 15–26.
[41] S. Meher, S. Nag, J. Tiley, A. Goel, R. Banerjee, Coarsening kinetics of γ′ precipitates in cobalt-base alloys, Acta Mater. 61 (2013) 4266–4276.
[42] A.M. Jokisaari, S.S. Naghavi, C. Wolverton, P.W. Voorhees, O.G. Heinonen, Predicting the morphologies of γ′ precipitates in cobalt-based superalloys, Acta Mater. 141 (2017) 273–284.
[43] W.C. Johnson, J.W. Cahn, Elastically induced shape bifurcations of inclusions, Acta Metall. 32 (1984) 1925–1933.
[44] W.C. Johnson, M.B. Berkenpas, D.E. Laughlin, Precipitate shape transitions during coarsening under uniaxial stress, Acta Metall. 36 (1988) 3149–3162.
[45] M.E. Thompson, C.S. Su, P.W. Voorhees, The equilibrium shape of a misfitting precipitate, Acta Metall. Mater. 42 (1994) 2107–2122.
[46] E.A. Marquis, D.N. Seidman, Coarsening kinetics of nanoscale Al3Sc precipitates in an Al–Mg–Sc alloy, Acta Mater. 53 (2005) 4259–4268.
[47] E.Y. Plotnikov, Z. Mao, S.-I. Baik, M. Yildirim, Y. Li, D. Cecchetti, R.D. Noebe, G. Martin, D.N. Seidman, A correlative four-dimensional study of phase-separation at the subnanoscale to nanoscale of a Ni-Al alloy, Acta Mater. 171 (2019) 306–333.
[48] C.L. Chiang, Statistical Methods of Analysis, World Scientific, Singapore, 2003.
[49] C. Booth-Morrison, J. Weninger, C.K. Sudbrack, Z. Mao, R.D. Noebe, D.N. Seidman, Effects of solute concentrations on kinetic pathways in Ni–Al–Cr alloys, Acta Mater. 56 (2008) 3422–3438.
[50] C. Booth-Morrison, Y. Zhou, R.D. Noebe, D.N. Seidman, On the nanometer scale phase separation of a low-supersaturation Ni–Al–Cr alloy, Philos. Mag. A 90 (2010) 219–235.
[51] J.A. Marqusee, J. Ross, Kinetics of phase transitions: theory of Ostwald ripening, J. Chem. Phys. 79 (1983) 373–378.
[52] P.J. Bocchini, C.K. Sudbrack, R.D. Noebe, D.N. Seidman, Temporal evolution of a model Co-Al-W superalloy aged at 650 °C and 750 °C, Acta Mater. 159 (2018) 197–208.
[53] V.A. Snyder, J. Alkemper, P.W. Voorhees, Transient Ostwald ripening and the disagreement between steady-state coarsening theory and experiment, Acta Mater. 49 (2001) 699–709.
[54] U. Tetzlaff, H. Mughrabi, Enhancement of the high-temperature tensile creep strength of monocrystalline nickel-base superalloys by pre-rafting in compression, in: T.M. Pollock, R.D. Kissinger, R.R. Bowman, K.A. Green, M. McLean, S. Olson, J.J. Schirra (Eds.), Superalloys 2000: Proceedings of the Ninth International Symposium on Superalloys, TMS, Seven Springs, PA, 2000.
[55] D. Locq, P. Caron, S. Raujol, F. Pettinari-Sturmel, A. Coujou, N. Clément, On the role of tertiary γ' precipitates in the creep behaviour at 700 °C of a PM disk superalloy, in: K.A. Green (Ed.), Superalloys 2004, TMS (The Minerals, Metals & Materials Society), Champion, PA, 2004, pp. 179–187.
[56] T. Osada, Y. Gu, N. Nagashima, Y. Yuan, T. Yokokawa, H. Harada, New quantitative analysis of contributing factors to strength of disk superalloys, in: E.S. Huron (Ed.), Superalloys 2012, TMS (The Minerals, Metals & Materials Society), Seven Springs, Pennsylvania, 2012, pp. 121–128.
[57] T.H. Courtney, Mechanical Behavior of Materials, second ed., McGraw Hill, Boston, 2000.
[58] A. Mottura, A. Janotti, T.M. Pollock, Alloying effects in the γ′ phase of Co-based superalloys, in: E.S. Huron (Ed.), Superalloys 2012, TMS (The Minerals, Metals & Materials Society), Seven Springs, Pennsylvania, 2012, pp. 685–693.
[59] M.S. Titus, Y.M. Eggeler, A. Suzuki, T.M. Pollock, Creep-induced planar defects in $L1_2$-containing Co- and CoNi-base single-crystal superalloys, Acta Mater. 82 (2015) 530–539.
[60] T. Krol, D. Baither, E. Nembach, The formation of precipitate free zones along grain boundaries in a superalloy and the ensuing effects on its plastic deformation, Acta Mater. 52 (2004) 2095–2108.
[61] Q. Liu, J. Coakley, D.N. Seidman, D.C. Dunand, Precipitate evolution and creep behavior of a W-free Co-based superalloy, Metall. Mater. Trans. 47 (2016) 6090–6096.
[62] P.J. Bocchini, C.K. Sudbrack, R.D. Noebe, D.C. Dunand, D.N. Seidman, Microstructural and creep properties of boron- and zirconium-containing cobalt-based superalloys, Mater. Sci. Eng. A 682 (2017) 260–269.
[63] M. Kolb, L.P. Freund, F. Fischer, I. Povstugar, S.K. Makineni, B. Gault, D. Raabe, J. Müller, E. Spiecker, S. Neumeier, M. Göken, On the grain boundary strengthening effect of boron in γ/γ′ Cobalt-base superalloys, Acta Mater. 145 (2018) 247–254.
[64] F. Xue, H.J. Zhou, Q.Y. Shi, X.H. Chen, H. Chang, M.L. Wang, Q. Feng, Creep behavior in a γ′ strengthened Co–Al–W–Ta–Ti single-crystal alloy at 1000°C, Scripta Mater. 97 (2015) 37–40.
[65] F. Xue, C.H. Zenk, L.P. Freund, M. Hoelzel, S. Neumeier, M. Göken, Double minimum creep in the rafting regime of a single-crystal Co-base superalloy, Scripta Mater. 142 (2018) 129–132.
[66] A.K. Singh, N. Louat, K. Sadananda, Dislocation network formation and coherency loss around gamma-prime precipitates in a nickel-base superalloy, Metall. Trans. A 19 (1988) 2965–2973.
[67] A. Epishin, T. Link, U. Brückner, P.D. Portella, Kinetics of the topological inversion of the γ/γ′-microstructure during creep of a nickel-based superalloy, Acta Mater. 49 (2001) 4017–4023.
[68] Pandat, Computherm LLC, Madison, 2016.
[69] PanCobalt Thermodynamic Database, Computherm LLC, Madison, 2014.
[70] Thermocalc 2016a, Thermo-Calc Software AB, Stockholm, Sweden, 2016.
[71] TCNI8 Ni-Based Superalloy Database, Thermo-Calc Software AB, Stockholm, Sweden, 2015.
[72] T.P. Gabb, R.L. Dreshfield, Superalloy data, in: C.T. Sims, N.S. Stoloff, W.C. Hagel (Eds.), Superalloys II, Wiley-Interscience, New York, NY, United States, 1987, pp. 575–597.